Simulation of Multiple-Receiver, Broadband Interferometric SAS Imagery

Alan J. Hunter, Michael P. Hayes, and Peter T. Gough

Acoustics Research Group,
Dept. Electrical and Computer Engineering,
University of Canterbury, New Zealand
{*a.hunter,m.hayes,p.gough*}*@elec.canterbury.ac.nz*

***Abstract*— Interferometric Synthetic Aperture Sonar (InSAS) is a technique for high-resolution, 3-dimensional underwater imaging. A significant problem in developing and testing InSAS algorithms is the difficulty in obtaining ground-truth data to compare with the reconstructed imagery / bathymetry. Thus, a reliable simulation model is a useful aid. Most SAS simulation models are based on a point-scatterer representation of the underwater scene. The point-scatterer model is computationally inefficient for simulating large, realistic scenes. Furthermore, effects such as aspect-dependent scattering, speckle, shadowing, and multiple-scattering are not replicated easily.**

In this paper we present an efficient model for the realistic simulation of multiple-receiver InSAS imagery. The model is based on a facet representation of the underwater scene. The field scattered by each facet is realised using statistics determined by the Kirchhoff method and occlusions and multiple-scattering are resolved by ray-tracing. The simulation of InSAS imagery is demonstrated using the parameters of our Kiwi-SAS system. The simulated imagery is shown to include the characteristic effects of aspect-dependent scattering, speckle, and shadowing.

I. Introduction

Synthetic Aperture Sonar (SAS) is an extension of the conventional side-looking sonar technique for higher resolution underwater imaging [1]. Interferometric SAS (InSAS) is a further extension of the technique whereby a vertical array of hydrophones is employed to resolve the three-dimensional bathymetry [2]. In addition to an interferometric array, current InSAS systems typically employ an along-track array of hydrophones to allow for increased mapping rates [3]. When developing algorithms for such multiple-receiver InSAS systems, ground-truth data is required to validate the reconstructed imagery. However, ground-truth is difficult to obtain in the underwater environment and thus, an accurate and efficient simulation model is a useful aid.

Simulation models developed for conventional sonar are insufficient for modeling InSAS imagery due to the assumption of incoherent processing and the use of narrow-beam and narrow-band approximations. A number of models have been developed in the Synthetic Aperture Radar (SAR) literature [4]. However, available SAS models are quite simplistic compared to these. Typically, SAS simulation models are based on a point-scatterer representation of the simulated scene. The point-scatterer model is computationally inefficient for simulating large, realistic scenes. This is compounded by the increased mapping rates of multiple-receiver systems. Moreover, effects such as aspect-dependent scattering, rough-surface scattering (speckle), shadowing, and multiple-scattering cannot be modeled easily using point-scatterers. It is becoming increasingly important to accurately model these effects. In particular, the correct modeling of image correlation properties is important for development of autofocus algorithms [5].

In this paper, we present a novel approach to the efficient 3-dimensional simulation of multiple-receiver, broadband InSAS imagery. The model uses a rough facet representation of the underwater scene. The large-scale roughness of the scene (i.e., the surfaces that are resolvable by the sonar) is decomposed into a collection of facets, while the small-scale roughness is approximated by an aspect-dependent phase-screen. The field scattered by each facet is realised using mean and auto-correlation functions that are determined using the Kirchhoff method [6], [7]. Occlusions and multiple-scattering are resolved using ray-tracing techniques and the imagery is obtained by evaluating and summing the responses from the insonified facets.

The theory is developed for a general facet shape and arbitrary roughness statistics in Section III and the simplified case of Gaussian surface statistics is explored in Section IV. In Section V, simulated imagery is presented using the parameters of our Kiwi-SAS system [8]. The simulated imagery is shown to demonstrate effects characteristic of real InSAS imagery including aspect-dependent scattering, speckle, and shadowing.

II. Background

Synthetic Aperture Sonar differs from conventional side-looking sonar in its utilisation of both the magnitude and phase of the acoustic response. By utilising the forward motion of the sonar platform, a larger aperture can be synthesised using a coherent summation of the echos at subsequent pings. Synthetic aperture processing allows apertures many times the size of the physical aperture to be generated. Consequently, improved range-independent azimuth resolution can be achieved [1]. Vertical and along-track multiple receiver arrays are employed to allow for bathymetric reconstruction using interferometry [2] and a faster mapping rate [3] respectively.

0-933957-31-9

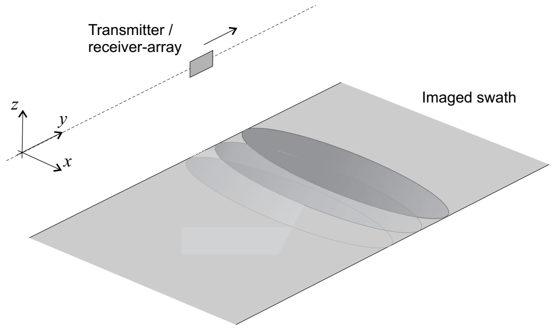

Fig. 1. The imaging geometry typical of a free-towed, multiple-receiver Synthetic Aperture Sonar in shallow-water.

The typical shallow-water imaging geometry for a free-towed InSAS is shown in Fig. 1. The sonar towfish travels roughly mid-water and insonifies a swath of the sea-floor along-side the towfish path (strip-map imaging). The swath is imaged at a low grazing-angle. Therefore, targets that are proud of the sea-floor cast shadows behind them. The shadow cast by a proud target can often provide further information of its structure.

Synthetic aperture processing and bathymetric reconstruction require a constant, linear tow-path. However since the platform is free-towed, it is susceptible to disturbances that can cause it to deviate from the ideal path. Autofocus techniques are required to correct the distortions in the imagery that are introduced by deviation from the ideal tow-path [5].

The swath is imaged using a widebeam, broadband, coherent source (e.g., a chirp signal). As with any coherent imaging process, this gives rise to speckle noise [9]. Speckle is a decorrelation of the scattered field due to constructive and destructive interference and is a result of rough-surface scattering. Due to the large azimuth beamwidth, targets are viewed from a wide range of angles. Generally, targets possess different scattering properties at different aspects and thus decorrelation is introduced. The decorrelation due to aspect-dependent scattering and speckle noise affects the performance of autofocus algorithms [5], [10] and imposes a fundamental limit on the interferometric phase accuracy for bathymetric reconstruction [11].

It is becoming increasingly important to model these effects that are characteristic of InSAS imagery. In the proposed simulation model, the decorrelation due to aspect-dependent scattering and speckle are represented using the Kirchhoff method. The ray-tracing technique is used to model shadowing, multiple-scattering, and refraction into semi-opaque scattering targets.

III. Scattering model

The acoustic back-scatter from an insonified target is, in general, due to a volume-scattering mechanism. This is particularly true of the sea-floor reverberation. However, we choose to consider back-scattering as the result of a surface-scattering mechanism. This simplifies the problem two-fold; since targets and the sea-floor/surface are easily described by surfaces and since surface-scattering is a simpler mechanism to model.

It is convenient to describe our underwater scenes using facets. A facet is a small polygon section of a planar surface. The surfaces in the scene are decomposed into a collection of facets and the response from these facets are determined and summed to produce the imagery. Each facet has properties that determine its scattering characteristics; these include the facet shape and orientation, roughness parameters, and a reflection coefficient. The scattering from each facet is described statistically using the Kirchhoff method and a realisation of the scattered field is generated using these statistics.

A. The Kirchhoff method for scattering from a rough facet

In the acoustic scattering model, the Kirchhoff method is used to approximate the statistics of the field scattered by a rough facet. The Kirchhoff method (also known as the tangent-plane method or the method of physical optics) is well-known and widely used for many rough-surface scattering problems [6], [7].

The Kirchhoff method is based upon two simplifying approximations: 1) At each point on the surface, the reflection coefficient is approximated by the reflection coefficient for a plane tangent to the surface at that point. 2) The field on the surface is approximated by the field that would exist in the absence of the scattering surface, i.e., the incident field. These assumptions are valid when the surface is smooth compared to a wavelength and when the scattering is weak, i.e., when multiple-scattering and shadowing can be neglected (the Born approximation).

Applying these approximations to the Kirchhoff-Helmholtz equation, the field scattered by a surface S is given by [7]

$$\begin{aligned}\Psi_s(\mathbf{x}, f) = \iint_S \Bigg[& (1-R)\ \frac{\partial}{\partial \hat{\mathbf{n}}} \Psi_i(\mathbf{x}', f)\, G(\mathbf{x}-\mathbf{x}', f) \\ & - (1+R)\ \Psi_i(\mathbf{x}', f)\, \frac{\partial}{\partial \hat{\mathbf{n}}} G(\mathbf{x}-\mathbf{x}', f) \Bigg]\ d\mathbf{x}',\end{aligned} \tag{1}$$

where Ψ_i is the incident field, $R = R(\mathbf{x})$ and $\hat{\mathbf{n}} = \hat{\mathbf{n}}(\mathbf{x})$ are, respectively, the reflection coefficient and surface normal for the plane tangent to the surface S, and G is the free-space Green's function given by

$$G(\mathbf{x}, f) = \frac{\exp(-jk|\mathbf{x}|)}{4\pi|\mathbf{x}|}, \tag{2}$$

where $|\cdot|$ denotes the Euclidean norm and $k = 2\pi f/c$ is the wavenumber.

The expression (1) can be simplified when the surface S is divided into two scales of roughness – a large-scale roughness, that is, the surfaces that are resolvable by the sonar, and a small-scale roughness, which is not resolvable yet still influences the scattered field. The large-scale roughness can be decomposed as a collection of facets, while the small-scale roughness can be approximated as an aspect-dependent phase-screen on these facets. The expression for the scattered field

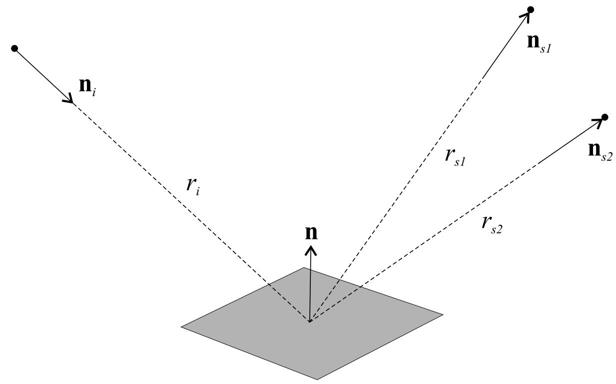

Fig. 2. The scattering geometry for a rough facet.

can be simplified further using the Fraunhoffer approximation by considering a single facet in the far-field of the acoustic source. The total scattered field is the sum of fields scattered by each insonified facet.

Using the geometry of Fig. 2, the field scattered by a rough facet is approximated in the far-field by

$$\begin{aligned}\Psi_s(\mathbf{x},f) = {} & \left[R\left(\hat{\mathbf{n}}_s+\hat{\mathbf{n}}_i\right)+\left(\hat{\mathbf{n}}_s-\hat{\mathbf{n}}_i\right)\right]\cdot\hat{\mathbf{n}} \\ & \times\ jk\ \frac{\exp\left(-jk\left(r_i+r_s\right)\right)}{(4\pi)^2\, r_i r_s}\ S(f)\, B(\mathbf{x},f)\,,\end{aligned} \tag{3}$$

where R is the average reflection coefficient, r_i and r_s are the distances from the centre of the facet to the respective source and field positions, and $\hat{\mathbf{n}}$, $\hat{\mathbf{n}}_i$, and $\hat{\mathbf{n}}_s$ are the facet, incident, and scattered normals respectively. S is the temporal spectrum of the transmitted signal and B is the facet beampattern given by

$$B(\mathbf{x},f) = \iint_{-\infty}^{\infty} w(\mathbf{x}')\exp\left(jk\ q_z h(\mathbf{x}')\right)\exp\left(jk\ \mathbf{q}_x\cdot\mathbf{x}'\right)\ d\mathbf{x}', \tag{4}$$

where $\mathbf{q}_x = (q_x, q_y)$ and $\mathbf{q} = (q_x, q_y, q_z) = \hat{\mathbf{n}}_s - \hat{\mathbf{n}}_i$. The aperture function w describes the facet shape, and the roughness function h describes the small-scale roughness. The beampattern integral (4) can be recognised as the Fourier transform of the product of the aperture function with the phase-screen $\exp\left(jk\ q_z h(\mathbf{x})\right)$.

B. Statistics of the field scattered by a rough facet

The beampattern of the scattered field (4) is dependent on the roughness function h. The roughness function is typically the realisation of a random process. Consequently, the resulting beampattern is also the realisation of a random process. Since the small-scale roughness is not resolvable by the sonar, it is sufficient to describe the roughness function statistically allowing for a statistical description of the beampattern and hence the scattered field.

The beampattern can be considered as the sum of a deterministic component and a random component. These are referred to as the specular (or coherent) and diffuse (or non-coherent) components respectively. The coherent and diffuse components of the beampattern are illustrated in Fig. 3. The coherent component is the mean of the beampattern and the diffuse component is the random variation about this mean, i.e.,

$$B(\mathbf{x},f) = B_c(\mathbf{x},f) + B_d(\mathbf{x},f)\,, \tag{5}$$

where

$$B_c(\mathbf{x},f) = \mathrm{E}\left\{B(\mathbf{x},f)\right\}, \tag{6}$$

$$B_d(\mathbf{x},f) = B(\mathbf{x},f) - B_c(\mathbf{x},f)\,, \tag{7}$$

are the coherent and diffuse components of the beampattern, and $\mathrm{E}\{\cdot\}$ denotes the ensemble average.

The coherent component is derived by taking the ensemble average of the beampattern expression (4), giving

$$B_c(\mathbf{x},f) = \Phi\left(-\frac{f}{c}q_z\right) W\left(-\frac{f}{c}\mathbf{q}_x\right), \tag{8}$$

where Φ is the characteristic function of the height distribution p, for the roughness function h, and W is the Fourier transform

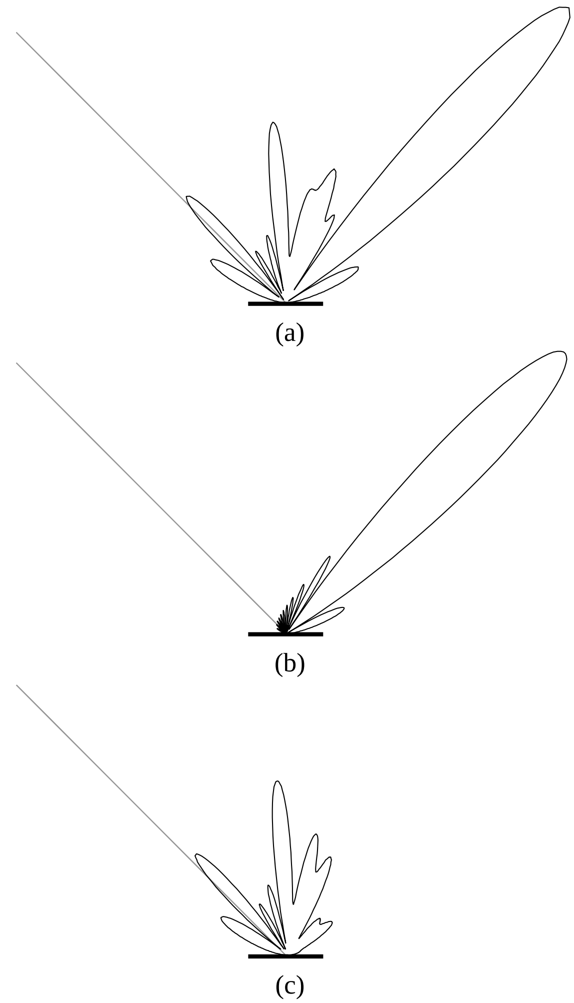

Fig. 3. The beampattern B of the field scattered by a rough facet is composed of coherent and diffuse components. The coherent component B_c, shown in (b) is the mean of the beampattern, while the diffuse component B_d, shown in (c) is the deviation about the mean.

of the aperture function w.

$$\Phi(\nu) = \int_{-\infty}^{\infty} p(\zeta) \exp(-j2\pi\zeta\nu)\ d\zeta \quad (9)$$

$$W(\mathbf{u}) = \iint_{-\infty}^{\infty} w(\mathbf{x}) \exp(-j2\pi\mathbf{x}\cdot\mathbf{u})\ d\mathbf{x} \quad (10)$$

The diffuse component of the beampattern is the realisation of a zero-mean random process. Neglecting higher-order components, the diffuse beampattern can be represented by its auto-correlation in space and time or temporal frequency. This auto-correlation is known as the Mutual Coherence Function (in space and time) or the Two-Frequency Correlation Function (in space and frequency). Here, we consider the Two-Frequency Correlation Function, defined by

$$\Gamma(\mathbf{x}_1, \mathbf{x}_2, f_1, f_2) = \mathrm{E}\left\{B_d(\mathbf{x}_1, f_1)\, B_d^*(\mathbf{x}_2, f_2)\right\}, \quad (11)$$

where $\cdot^*$ denotes complex conjugation.

From the beampattern expression (4), and the definition (11), the correlation function is given by

$$\begin{aligned}
&\Gamma(\mathbf{x}_1, \mathbf{x}_2, f_1, f_2) = \\
&\iiiint_{-\infty}^{\infty} w(\mathbf{x}_1')\, w^*(\mathbf{x}_2')\, \Phi\left(-\frac{f_1}{c}q_{z1}, \frac{f_2}{c}q_{z2}, \mathbf{x}_1', \mathbf{x}_2'\right) \\
&\times\ \exp\left(-j2\pi\left(\frac{f_2}{c}\mathbf{q}_{x2}\cdot\mathbf{x}_2' - \frac{f_1}{c}\mathbf{q}_{x1}\cdot\mathbf{x}_1'\right)\right)\ d\mathbf{x}_1'\ d\mathbf{x}_2',
\end{aligned} \quad (12)$$

where

$$\begin{aligned}
\Phi(\nu_1, \nu_2, \mathbf{x}_1, \mathbf{x}_2) = &\iint_{-\infty}^{\infty} p(\zeta_1, \zeta_2, \mathbf{x}_1, \mathbf{x}_2) \\
&\times\ \exp(-j2\pi(\nu_1\zeta_1 + \nu_2\zeta_2))\ d\zeta_1\ d\zeta_2
\end{aligned} \quad (13)$$

is the characteristic function of the bivariate height distribution p, for the roughness function h.

IV. Realisation of the scattered field

A realisation of the scattered field can be made by substitution of a beampattern realisation into the expression for the scattered field (3). In general, the coherent component of the beampattern and the correlation function of the diffuse component are difficult to evaluate. However, for certain aperture functions and roughness statistics, closed-form solutions can be obtained. We consider quadrilateral and triangular shaped facets (aperture functions), since any surface can be tessellated using these shapes. For the statistics of the roughness function, we assume a zero-mean, Gaussian distribution, and a circular, Gaussian correlation function.

A. *Scattering from a rough facet with Gaussian statistics*

For a 2-dimensional, random process with a zero-mean, Gaussian distribution and a circular, Gaussian correlation function, the characteristic functions are given by

$$\Phi(\nu) = \exp\left(-2\pi^2\sigma^2\nu^2\right) \quad (14)$$

and

$$\begin{aligned}
&\Phi(\nu_1, \nu_2, \mathbf{x}_1, \mathbf{x}_2) = \\
&\quad \exp\left(-2\pi^2\sigma^2\left[\nu_1^2 + \nu_2^2 + 2\nu_1\nu_2\ C(\mathbf{x}_2 - \mathbf{x}_1)\right]\right),
\end{aligned} \quad (15)$$

where σ^2 is the variance and

$$C(\mathbf{x}) = \exp\left(-\frac{|\mathbf{x}|^2}{l^2}\right), \quad (16)$$

where l is the correlation length.

The coherent component of the beampattern can be obtained by substitution of the characteristic function (14) into the expression (8), giving

$$B_c(\mathbf{x}, f) = \exp\left(-2\pi^2\sigma^2\left(\frac{f}{c}q_z\right)^2\right) W\left(-\frac{f}{c}\mathbf{q}_x\right). \quad (17)$$

The coherent component is a scaled Fourier transform of the aperture function. This result is intuitively satisfying, since the coherent component decreases to zero as the variance, frequency, or angle of incidence are increased.

The correlation function Γ is obtained by substitution of the characteristic function (15) into the expression (12). The resultant expression is complicated due to the double exponential and is, in general, difficult to evaluate analytically. By assuming the correlation length l is smaller than the facet extent a simpler form can be obtained. Letting $l \to 0$, the characteristic function approaches

$$\Phi(\nu_1, \nu_2, \mathbf{x}_1, \mathbf{x}_2) = \exp\left(-2\pi^2\sigma^2\left(\nu_1^2 + \nu_2^2\right)\right)\delta_k(\mathbf{x}_2 - \mathbf{x}_1), \quad (18)$$

where δ_k is the Kronecker delta-function. However, the expression (12) is found to equate to zero upon substitution of (18) in this limiting case. This is the result of a breakdown in the Kirchhoff method, whereby the scattered field has only evanescent modes. To alleviate this problem, a heuristic normalisation [12] can be applied by assuming the evanescent waves are re-radiated as propagating modes due to multiple-scattering on the facet surface. Under this assumption, the Kronecker delta-function is replaced by a Dirac delta-function, giving

$$\begin{aligned}
&\Gamma(\mathbf{x}_1, \mathbf{x}_2, f_1, f_2) = \\
&\quad \exp\left(-2\pi^2\sigma^2\left[\left(\frac{f_1}{c}q_{z1}\right)^2 + \left(\frac{f_2}{c}q_{z2}\right)^2\right]\right) \\
&\quad \times\ R_w\left(\frac{f_2}{c}\mathbf{q}_{x2} - \frac{f_1}{c}\mathbf{q}_{x1}\right)
\end{aligned} \quad (19)$$

where

$$R_w(\mathbf{u}) = \iint_{-\infty}^{\infty} |w(\mathbf{x})|^2 \exp(-j2\pi\ \mathbf{u}\cdot\mathbf{x})\ d\mathbf{x} \quad (20)$$

is the auto-correlation of the facet aperture function.

A realisation of the diffuse beampattern component can be made using the correlation function Γ. Using the central limit theorem, the real and imaginary parts of the diffuse component assume independent Gaussian distributions when the number of independent scattering points is large [9]. Consequently, the amplitude is Rayleigh-distributed and the phase is uniform-distributed. This assumption is valid since the surface correlation length is considered small. Approximating the exponential amplitude term in (19) by a constant, the correlation function Γ describes a stationary process in the angular wavenumber domain. Thus, a realisation can be made by filtering a complex, Gaussian-distributed, white noise process with the filter described by the auto-correlation function (19).

B. Occlusions and multiple-scattering

The method described so far has neglected shadowing and multiple-scattering on the surface of each facet. This is justified since roughness of this scale cannot be resolved. However, it is important to note that occlusion and multiple-scattering of the small-scale roughness does affect the statistical properties of the scattered field.

To resolve large-scale occlusions and multiple-scattering, the ray-tracing technique is employed. For each position along the path, a ray is traced from the transmitter to each facet and back to each receiver. Intersection calculations are performed to determine if a facet is obstructed. If so, the response of the occluded facet is not included in the total scene response. For strong-scattering facets, the insonified facet acts as a new acoustic source and the ray-tracing process continues recursively. Ray-tracing is a computationally intensive process, especially when multiple-scattering is considered. In order to reduce computational costs common speed-up techniques are used, including the use of bounding spheres and back-face culling [13].

V. Results

To demonstrate the performance of the proposed simulation model, a scene is simulated using the parameters of the Kiwi-SAS system [8]. The Kiwi-SAS operates in two frequency bands 20–40kHz and 90–110kHz, giving a range resolution of 35mm in each band. The interferometric receiver array consists of three vertically displaced hydrophones of dimensions 300mm x 75mm, giving a theoretical along-track resolution of 150mm after synthetic aperture reconstruction.

The scene consists of a 1m diameter sphere resting on a flat sea-floor. The sphere is situated 30m from the tow-path, which is 5m above the sea-floor. The sea-floor is modeled using 3000 square facets and the sphere is modeled using 200 triangular facets. The facets have a unity reflection coefficient and are rough comparable to a wavelength at 30kHz. The scene is simulated for the top and bottom receivers in the 30kHz band. The raw, pulse-compressed imagery is shown in Fig. 4 (a), while Fig. 4 (b) shows the synthetic aperture reconstruction.

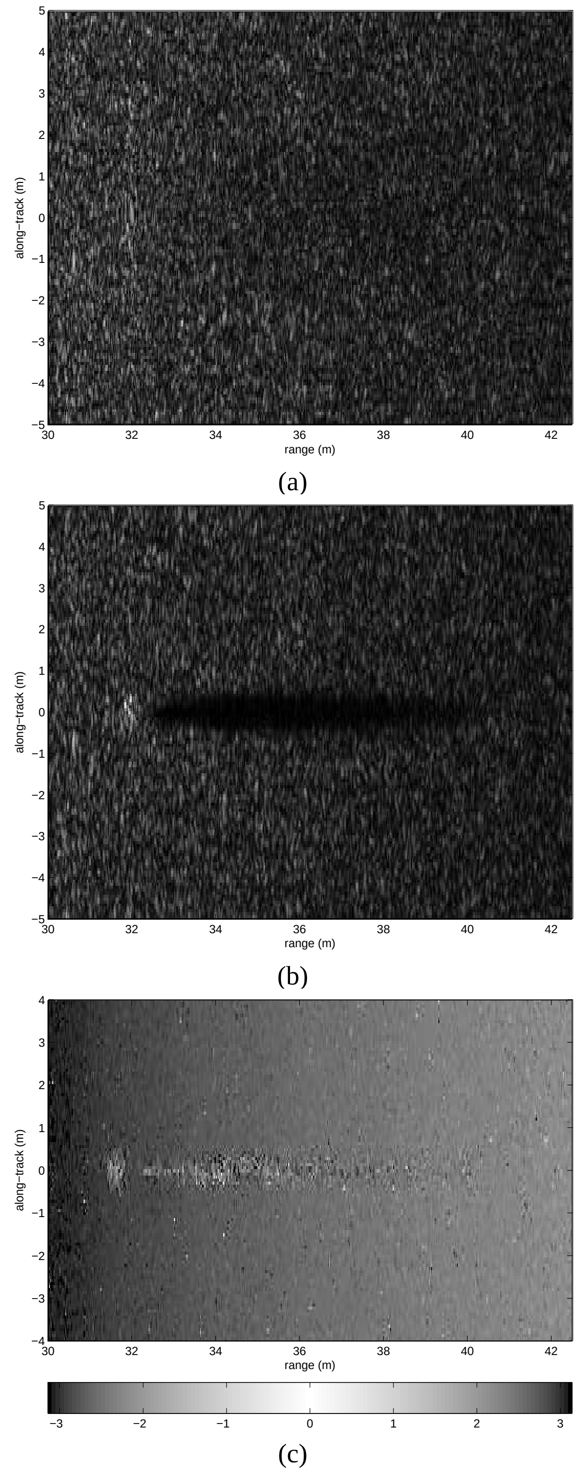

Fig. 4. Simulated imagery of a 1m diameter sphere on a flat sea-floor: For the top receiver in the interferometric array, (a) shows the pulse-compressed imagery and (b) shows the synthetic aperture reconstruction. The interferogram between the top and bottom receivers is shown in (a).

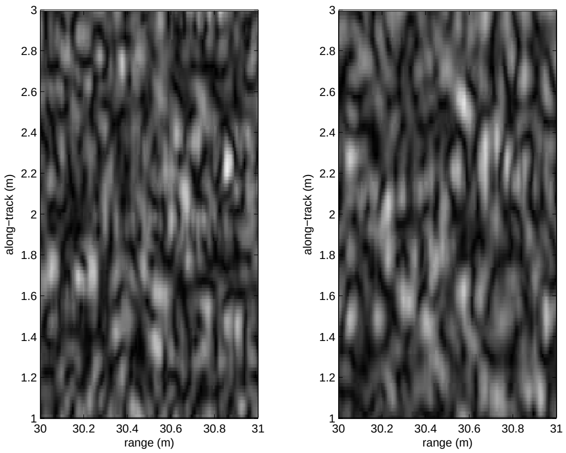

(a) (b)

Fig. 5. Enlargement of a section of the seafloor clutter from (a) pulse-compressed, and (b) reconstructed simulated data.

The sphere target can be seen only faintly in the pulse-compressed imagery, but is quite apparent in the reconstructed imagery. The shadow behind the sphere is not visible in the pulse-compressed imagery, but is very prominent after reconstruction. Fig. 4 (c) shows the interferogram between the two receivers. The gentle gradient due to the changing phase difference is apparent and a sudden phase change can be seen due to the sphere target. An enlargement of the sea-floor clutter is shown in Fig. 5, where the speckle size is seen to be commensurate with the sonar resolution as expected.

VI. Conclusions

An efficient model for the realistic simulation of multiple-receiver, broadband InSAS imagery has been presented. It has been shown to replicate characteristics of real InSAS imagery such as aspect-dependent scattering, speckle, and shadowing, providing a reliable means of obtaining ground-truth information for the further development of InSAS algorithms.

The presented model is an improvement over the point-scatterer model. However, it is based on a number of simplifying assumptions and approximations. The Kirchhoff method is only valid for surfaces that are smooth compared to the wavelength. This assumption is violated due to the small-scale roughness. Also, shadowing and multiple-scattering are neglected at the small-scale. The facet beampatterns are derived assuming a far-field source, which is not always true when multiple-scattering occurs within a target. Diffraction effects have also been neglected. The degree to which these assumptions and approximations are violated increases at low grazing angles and frequencies, which is where SAS systems typically operate. Future work will concentrate on correcting some of these violations, while retaining computational efficiency.

Acknowledgment

Alan Hunter thanks the University of Canterbury for his Doctoral Scholarship.

References

[1] D. W. Hawkins, "Synthetic aperture imaging algorithms: with application to wide bandwidth sonar." Ph.D. dissertation, Department of Electrical and Electronic Engineering, University of Canterbury, October 1996.

[2] P. J. Barclay, M. P. Hayes, and P. T. Gough, "Reconstructing seafloor bathymetry with a multichannel broadband InSAS," in *OCEANS 2003*. San Diego, CA: IEEE, September 2003.

[3] H. J. Callow, M. P. Hayes, and P. T. Gough, "Wavenumber domain reconstruction of SAR/SAS imagery using single transmitter and multiple-receiver geometry," *Electronics Letters*, vol. 38, no. 7, pp. 336–338, March 2002.

[4] G. Franceschetti, A. Iodice, M. Migliaccio, and D. Riccio, "A novel across-track SAR interferometry simulator," *IEEE Trans. Geoscience and Remote Sensing*, vol. 36, no. 3, pp. 950–962, May 1998.

[5] H. J. Callow, "Signal processing for Synthetic Aperture Sonar image enhancement," Ph.D. dissertation, Department of Electrical and Computer Engineering, University of Canterbury, April 2003.

[6] P. Beckmann and A. Spizzichino, *The Scattering of Electromagnetic Waves from Rough Surfaces*. Artech House, 1987.

[7] J. A. Ogilvy, *Theory of Wave Scattering from Random Rough Surfaces*. Adam Hilger, 1991.

[8] M. P. Hayes, P. J. Barclay, P. T. Gough, and H. J. Callow, "Test results of a bathymetric Synthetic Aperture Sonar," in *OCEANS 2001*. Hawaii: IEEE, November 2001.

[9] J. C. Dainty, Ed., *Laser Speckle and Related Phenomena*, ser. Topics in Applied Physics. Springer-Verlag, 1975, vol. 9.

[10] S. A. Fortune, M. P. Hayes, and P. T. Gough, "Contrast optimisation of Synthetic Aperture Sonar images," in *OCEANS 2003*. San Diego, CA: IEEE, September 2003.

[11] H. Zebker and J. Villasenor, "Decorrelation in interferometric radar echos," *IEEE trans. Geoscience and Remote Sensing*, vol. 30, no. 5, pp. 950–959, September 1992.

[12] J. E. Harvey, C. L. Vernold, A. Krywonos, and P. L. Thompson, "Diffracted radiance: a fundamental quantity in nonparaxial scalar diffraction theory," *Applied Optics*, vol. 38, no. 31, pp. 6469–6481, November 1999.

[13] J. D. Foley, A. van Dam, S. K. Feiner, and J. F. Hughes, *Computer Graphics: Principles and Practice*, 2nd ed. Addison-Wesley, 1997.